communications physics

A Nature Portfolio journal

Article

https://doi.org/10.1038/s42005-026-02685-6

Rise and fall of the pseudogap in the Emery model, insights for cuprates

Check for updates

M. O. Malcolms [1] ✉, Henri Menke [1,2], Yi-Ting Tseng [2], Eric Jacob [3], Karsten Held [3], Philipp Hansmann [2,4] & Thomas Schäfer [1,5] ✉

The pseudogap in high-temperature superconducting cuprates is an exotic state of matter, displaying emerging Fermi arcs and a momentum-selective suppression of spectral weight upon cooling. We show how these phenomena are captured in the three-band Emery model by performing dynamical vertex approximation calculations for its normal state. For the hole-doped parent compound, our results demonstrate the formation of a pseudogap due to short-ranged commensurate antiferromagnetic fluctuations. At larger doping values, progressively, incommensurate correlations and a metallic regime appear. Our results are in qualitative agreement with this doping trend in the normal state of cuprates, and hence, represent a step towards the uniform description of their phase diagrams within a single theoretical framework.

The intriguing properties of layered cuprate superconductors remain as fascinating today as at their discovery in 1986 by Bednorz and Müller[1]. The reason for the unbroken interest is at least three-fold: First, their temperature/doping phase diagram is unusually rich[2], exhibiting quantum magnetism, unconventional superconductivity, strange metallicity and the famous pseudogap regime, as a function of temperature and (hole-)doping. Second, cuprates hold the potential for immensely impactful technological applications of high-temperature superconductivity. Third, the physical mechanisms behind this rich phenomenology are – after almost 40 years of intense community effort– still highly debated. The reason for the latter is deeply rooted in the fact that cuprates are strongly interacting quantum many-body systems, whose properties cannot be explained by a simple single-particle picture: their electrons are strongly correlated in space and in time.

Adding to the complexity of this material class, it has been realized early on that, due to the close vicinity of the oxygen p-orbitals to the Fermi level, the oxygen $p_{x/y}$-orbitals of the CuO_2 two-dimensional layers are relevant besides the copper $d_{x^2-y^2}$-orbitals; and that the undoped parent compounds are charge-transfer, rather than (single-orbital) Mott-Hubbard insulators[3]. In order to explicitly include charge-transfer processes, the minimal model thus has to treat the oxygen p- on top of the copper d-orbitals, enabling, among other properties, (Zhang-Rice) singlet-formation between these orbitals[4]. These considerations led to the famous three-band model proposed by Emery[5], Varma, Schmitt-Rinks, and Abrahams[6] and later refined by Andersen and coworkers[7]. In this respect, the situation in cuprates is largely differing from the case of the recently discovered infinite-layer nickelate superconductors[8]. For the latter case, first-principle-based calculations indicate that indeed a single-band Hubbard model could suffice for the low-energy description of superconductivity and a putative pseudogap[9,10]; for recent reviews on the single-band Hubbard model see refs. 11,12.

One of the hallmark features of the normal state of the cuprates is the so-called pseudogap, a suppression of the spectral function near the antinode $(\pi, 0)$ at low hole-doping levels, cf. Fig. 1. This intriguing regime, which shows no signs of a thermodynamic phase transition, can be directly detected by angle-resolved photoemission spectroscopy (ARPES) experiments[13–19], and coincides with the peculiar behavior of the nuclear magnetic resonance (NMR) Knight shift[20].

A reliable modeling of cuprates, not only has to take into account their multi-orbital nature, but should also be able to reveal the crossover into the pseudogap regime upon hole doping. While the pseudogap in the Hubbard model has been firmly established by numerous approaches[21–26], the presence and nature of the pseudogap in the hole-doped Emery model has been, to the best of our knowledge, not thoroughly investigated yet: Despite efforts with a variety of techniques[27–34] and calculations for the superconducting properties[35–37], a detailed analysis of the evolution of the Fermi surface with temperature and doping, and its connection to the precise nature of spin fluctuations, essential hallmarks of the pseudogap regime, have not been reported before.

In this work, we now make significant progress in the universal description of the cuprate phase diagram by extending the state-of-the-art λ-corrected dynamical vertex approximation (DΓA) to the three-band Emery model (see Supplementary Note 2 of the Supplementary Information and ref. [38]). With our extension to three bands and arbitrarily accurate resolution

[1]Max-Planck-Institut für Festkörperforschung, Stuttgart, Germany. [2]Department of Physics, Friedrich-Alexander-Universität Erlangen/Nürnberg, Erlangen, Germany. [3]Institute of Solid State Physics, TU Wien, Vienna, Austria. [4]Science Institute and Faculty of Physical Sciences, University of Iceland, Reykjavík, Iceland. [5]Dipartimento di Fisica, Universitá di Trieste, Trieste, Italy. ✉e-mail: m.deoliveira@fkf.mpg.de; t.schaefer@fkf.mpg.de

of momenta and correlation lengths we establish the normal phase regime of the Emery model in two dimensions with realistic cuprate parameters as a function of temperature and hole doping. We document the fate of the pseudogap from its rise out of the insulating parent compound to its eventual fall in the metallic regime (see Fig. 1). We further discuss the relevance of our calculations for spectroscopic experiments, a crucial step on the way to a comprehensive theoretical description of the cuprates.

Results

Model and methods

We consider the three-band Emery model that accounts for the copper-oxygen hybridized character of the single band that crosses the Fermi surface and whose Hamiltonian reads

$$H = \sum_{\mathbf{k},\sigma} \psi^{\dagger}_{\mathbf{k},\sigma} \bar{h}_0(\mathbf{k}) \psi_{\mathbf{k},\sigma} + U \sum_i n^d_{i,\uparrow} n^d_{i,\downarrow}, \tag{1}$$

where $\psi^{\dagger}_{\mathbf{k},\sigma} = (d^{\dagger}_{\mathbf{k},\sigma}, p^{\dagger}_{x,\mathbf{k},\sigma}, p^{\dagger}_{y,\mathbf{k},\sigma})$ contains the electronic creation operators on the copper $d_{x^2-y^2}$- and the oxygen p_x- and p_y-orbitals with spin σ and momentum $\mathbf{k}$. U quantifies the local part of the Coulomb repulsion restricted to the copper $d_{x^2-y^2}$-orbital and $n^d_{i,\sigma} = d^{\dagger}_{i,\sigma} d_{i,\sigma}$ is the number operator per spin for the d-orbital. On the square lattice, setting the distance between unit cells to unity, the non-interacting Hamiltonian $\bar{h}_0(\mathbf{k})$ in Eq. (1) reads

$$\bar{h}_0(\mathbf{k}) = \begin{pmatrix} \epsilon_d & t_{pd} s_{k_x} & t_{pd} s_{k_y} \\ t_{pd} s^*_{k_x} & \epsilon_p + t'_{pp} \varepsilon_{k_x} & t_{pp} s^*_{k_x} s_{k_y} \\ t_{pd} s^*_{k_y} & t_{pp} s^*_{k_y} s_{k_x} & \epsilon_p + t'_{pp} \varepsilon_{k_y} \end{pmatrix}, \tag{2}$$

with $\varepsilon_k = 2\cos k$ and $s_k = 2ie^{i\frac{k}{2}} \sin\frac{k}{2}$. The on-site energies on the Cu and O orbitals are denoted ϵ_d and ϵ_p, respectively. The nearest-neighbor Cu-O hopping is denoted by t_{pd}, while t'_{pp} and t_{pp} denote the direct nearest-neighbor O-O hopping and the indirect one through the Cu site, respectively.

In our calculations, following Refs. 35,39,40, we adopt $t_{pp} \sim 650$ meV, $\epsilon_p = 2.3 t_{pp} = 1.5$ eV, $t_{pd} = 2.1 t_{pp} = 1.37$ eV and $t'_{pp} = 0.2 t_{pp} = 130$ meV for the non-interacting system in Eq. (2); ϵ_p has been obtained by subtracting the same double-counting contribution as in Ref. 39. Motivated by X-ray photoemission spectroscopy (XPES) experiments[41,42], in this work, we fix the interaction value to $U = 10 t_{pp} = 6.5$ eV, while the total electronic density $n = n_{d_{x^2-y^2}} + n_{p_x} + n_{p_y}$ and the temperature T are varied.

We analyze the normal state of the model by means of ladder DΓA[43], a diagrammatic extension[44] of the dynamical mean-field theory[45] which is particularly suited for treating spatial and temporal correlations. Specific properties of this method are its arbitrarily high momentum resolution and applicability in the strong-coupling regime, both of which being (i) highly desired for the description of the pseudogap regime and (ii) of advantage over cluster (see, e.g.,[28,29,32,34–37,40,46]) or other diagrammatic (see, e.g.,[31]) techniques, respectively. As such, DΓA has already been very successful for single-band systems over the past years[9,23,44,47]. We now extend this method to the Emery model (see Supplementary Information).

Fermi surfaces, Fermi arcs, and spectral functions

We first investigate the hole-doping and temperature evolution of the electronic spectrum. Figure 2a displays the the Green function at different momenta in imaginary time $\tau = \beta/2$ $(\beta = 1/T)$ for different temperatures: T = 377 K, 251.33 K and various values of hole-doping: δn = 0.00, 0.05, 0.10, 0.15, 0.20 with $\delta n = 5 - n$. It is directly related to the spectrum in an energy interval $\sim T$ around the Fermi energy, $-\frac{\beta}{\pi} G(\mathbf{k}, \tau = \beta/2) = \frac{\beta}{2\pi} \int \mathrm{d}\,\omega \frac{A(\mathbf{k},\omega)}{\cosh(\beta\omega/2)}$, and avoids the perils of the ill-conditioned analytical continuation.

Figure 2a also displays the correlated Fermi plus Luttinger surface, indicated as dashed white lines and determined as $\mathrm{Re}\, G(\mathbf{k}_{\mathrm{FS}}, i\omega_n \to 0) = 0$, where $i\omega_n \to 0$ is obtained as a linear extrapolation of the two first fermionic Matsubara frequencies. The minima (maxima) of $-\frac{\beta}{\pi} G(\mathbf{k}_{\mathrm{FS}}, \tau = \beta/2)$ on the correlated Fermi surface defines the anti-nodal (nodal) point indicated by the orange (red) dot (square) in Fig. 2(a). For both temperatures, T = 377 K and 251.33 K, the electronic spectrum evolves upon doping from an insulating parent compound (undoped system, δn=0.00) characterized by a very low spectral intensity over the Fermi surface into a metallic regime (δn=0.20). In between, a pseudogap phase, marked by the appearance of a Fermi arc structure at the Fermi level, emerges (δn = 0.10), which is a hallmark feature of cuprates[15]. Upon cooling, the spectrum intensity over the Fermi surface reduces for the undoped system while it increases for the highest doping analyzed here ($\delta n = 0.20$), which documents the evolution of the system from an insulating into a metallic state upon hole-doping. In addition, from δn = 0.05 to δn = 0.10 in Fig. 2(a), for both temperatures T = 377 K and 251.33 K, the reduction in the scattering processes between the quasiparticles leads to a topological reconstruction of the Fermi surface from an electron-like to a hole-like shape (Lifshitz transition)[22,48]. At higher hole-doping levels ($\delta n \geq 0.3$), an (inverse) Lifshitz transition emerges and the Fermi surface undergoes a change from a hole-like to an electron-like shape. This inverse transition is well described by only including local (quantum) fluctuations (see Supplementary Note 9 in the Supplementary Information for a more detailed discussion). For δn = 0.00 (insulating state) no Fermi surface can be defined, since the system is completely gapped.

In Fig. 2a, we further observe that even deep inside the metallic state ($\delta n = 0.20$), non-local correlation effects alter the Fermi surface (see Fig. S8 in the Supplementary Information for a comparison with DMFT). These changes in the Fermi surface arise from the momentum dependence of the real part of the electronic self-energy ($\mathrm{Re}\,\Sigma_{\mathbf{k},i\omega_n}$) and are minor compared to the much more dramatic opening of the pseudogap at the antinode. Instead, this pseudogap opening is due to the momentum dependence of $\mathrm{Im}\,\Sigma_{\mathbf{k},i\omega_n}$ and can severely affect superconducting instabilities as previously shown[49].

Figure 2b shows the doping evolution of the nodal (upper panel) and anti-nodal (lower panel) spectral weight for different temperatures. For the undoped system we observe that upon cooling the spectral weight at both node and anti-node decreases, corroborating the notion of an insulating regime. However, in δn = 0.05, while the spectral function at the antinodal point still decreases upon cooling, it saturates at the nodal point. This behavior indicates a crossover into the pseudogap phase, since at a higher doping δn = 0.10 the spectral function at the nodal point shows the inverse behavior of the antinodal one. That is, it increases now upon decreasing temperature indicating the metallicity of the nodal point. With further doping to δn = 0.15, a saturation at the antinodal point is also observed. This point introduces a second crossover into a metallic phase for all momenta that can be observed at δn = 0.20, where both spectral weights at node and antinode increase when cooling the system, the characteristic feature of a metal.

To investigate in greater depth the crossovers observed from the Green function on the Matsubara axis, in Fig. 3, we present the low-frequency behavior of the analytically continued spectral function (left panel) at points of the Brillouin zone where the spectral function at the Fermi level reaches its maximum (right panel). We obtain the real-frequency spectral function by performing the MaxEnt analytical continuation[50] of the lattice Green function at T = 251.33 K for the relevant hole-doping levels δn = 0.0, 0.10 and 0.20. The undoped system (δn = 0.00) [Fig. 3(a)] clearly displays an insulating behavior marked by the presence of a complete gap at the Fermi level. In the pseudogap phase (δn = 0.10), Fig. 3(b) shows the appearance of Fermi arcs where the spectral function is strongly momentum dependent and does not extend to the edges of the Brillouin zone (BZ). In addition, Fig. 3b also shows that along the Fermi arc coherent nodal states are located along the ΓM-direction, while the completely gapped antinodal ones are located along the XM-direction. In contrast to the pseudogap regime, in the metallic phase (Fig. 3c) the spectral function extends to the edges of the BZ. Moreover, in the metallic phase, the maximum of the spectral function at the Fermi level still displays a sizable momentum dependence over the Brillouin zone with incoherent states located close to edges of the BZ.

Magnetic susceptibilities and correlation lengths

An interesting question is whether the pseudogap phase is driven by spin fluctuations (see, for instance, refs. [51,52]), as demonstrated for the single-band Hubbard model by fluctuation diagnostics techniques[53–55]. Figure 4b shows the doping dependence of the magnetic correlation length ξ obtained by an Ornstein-Zernike fit of the static magnetic lattice susceptibility $\chi(\mathbf{q}, 0) = \chi(\mathbf{q}, i\Omega_n = 0)$ for different temperatures. Note that, as we consider an ideal two-dimensional system, neither the magnetic correlation length nor the static magnetic lattice susceptibility diverge at finite temperatures[56]. For all temperatures in Fig. 4b, the magnetic correlation length rapidly decreases upon hole-doping, reaching always its maxima in the undoped system ($\delta n = 0.00$). Differently from the undoped system where the insulating phase seems to be driven by long-ranged spin fluctuations characterized by a large correlation length (~ 70 sites at $T = 188.50$ K), deep inside the pseudogap phase ($\delta n = 0.10$) the magnetic correlation is rather small ($\lesssim 5$ lattice sites at $T = 251.33$ K) and only slightly varying with temperature and doping. This indicates that the opening of the pseudogap regime in the Emery model is driven by short-ranged dynamical spin fluctuations included in the ladder DΓA construction of the electronic self-energy (see Supplementary Note 2 of the Supplementary Information).

To extend our analysis, Fig. 4a displays the doping and temperature dependence of $\chi(\mathbf{q}, 0)$ over the Brillouin zone. For all temperatures, at low hole-doping ($\delta n < 0.15$) where the system is either insulating or in the pseudogap regime, the antiferromagnetic correlations are commensurately peaked at $\mathbf{q} = \mathbf{M} = (\pi, \pi)$, while inside the metallic phase ($\delta n \geq 0.15$) they become incommensurate and peak at $\mathbf{q} = (\pi, \pi \pm \delta), (\pi \pm \delta, \pi)$. In addition, Fig. 4c shows the temperature and doping dependence of the uniform susceptibility $\chi_{sp}(\mathbf{0}, 0)$. According to the Mila-Rice-Shastry model[57,58], the uniform spin susceptibility is directly proportional to the Knight shift measured in NMR experiments. From Fig. 4c, we observe that in the correlated metallic regime, at large hole-doping ($\delta n = 0.2$), $\chi_{sp}(\mathbf{0}, 0)$ monotonically increases upon cooling. In contrast, decreasing the hole-doping level towards the insulating undoped regime, $\chi_{sp}(\mathbf{0}, 0)$ displays a maximum at a temperature T^*_χ. In particular, as the electronic density increases from $\delta n = 0.15$ to $\delta n = 0.00$, T^*_χ gradually increases to higher temperatures (see Fig. S7 of the Supplementary Information). For all temperatures, the overall magnitude of the uniform spin susceptibility increases upon decreasing the hole-doping.

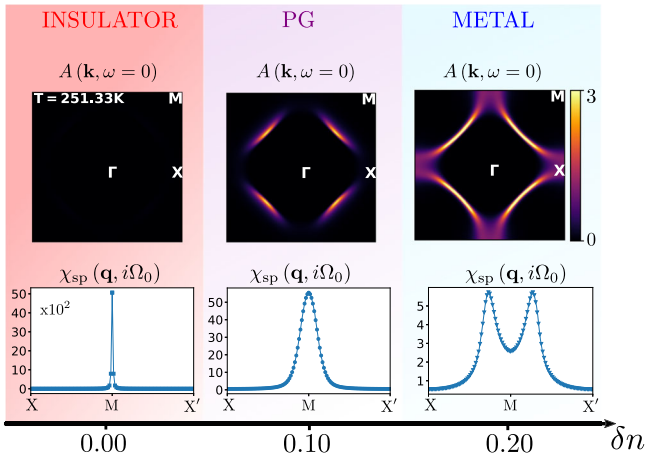

Fig. 1 | Sketch of the different normal phases of the three-orbital Emery model for cuprates as a function of hole doping δn, for a fixed temperature $T = 251.33$ K and as actually calculated by the dynamical vertex approximation. After an insulating regime the pseudogap (PG) first rises and then falls off again with the system eventually becoming a conventional metal. In the PG regime, the Fermi surface is reduced to Fermi arcs (upper panel, the high-symmetry points are $\Gamma = (0, 0)$, X $= (\pi, 0)$ and M $= (\pi, \pi)$). Concomitantly, commensurate antiferromagnetic and incommensurate magnetic fluctuations are present, demonstrated by the momentum-dependent spin susceptibility (lower row). The shadings serve as a guide to the eye throughout the manuscript.

Discussion

We now compare our results with experimental studies for one of the most prominent members of the cuprate family: $La_{2-x}Sr_xCuO_4$ (LSCO). The model parameters used for our calculations fit reasonably well with the parameters determined for LSCO previously by ab-initio methods[39], except for ε_p, which is slightly smaller in our study. For LSCO a large number of experimental studies that connect to our Emery model calculation in the paramagnetic phase exist: the evolution of the Fermi surface, the nature of the magnetic fluctuations, and the magnetic correlation length have been measured as a function of Sr-doping, corresponding to hole-doping in our calculations. Also, measurements of the spin susceptibility in LSCO is representative for other cuprates[59]. In the following, we assume a clean system, see ref. [60] for a recent review of the impact of disorder on the cuprates' phase diagram.

For the lowest temperatures that we analyzed, we find the pseudogap regime in a doping range of $\delta n \in [0.05, 0.15]$. This is in good agreement with the ARPES[61–63] and Nernst effect[64] measurements. The underlying Fermi

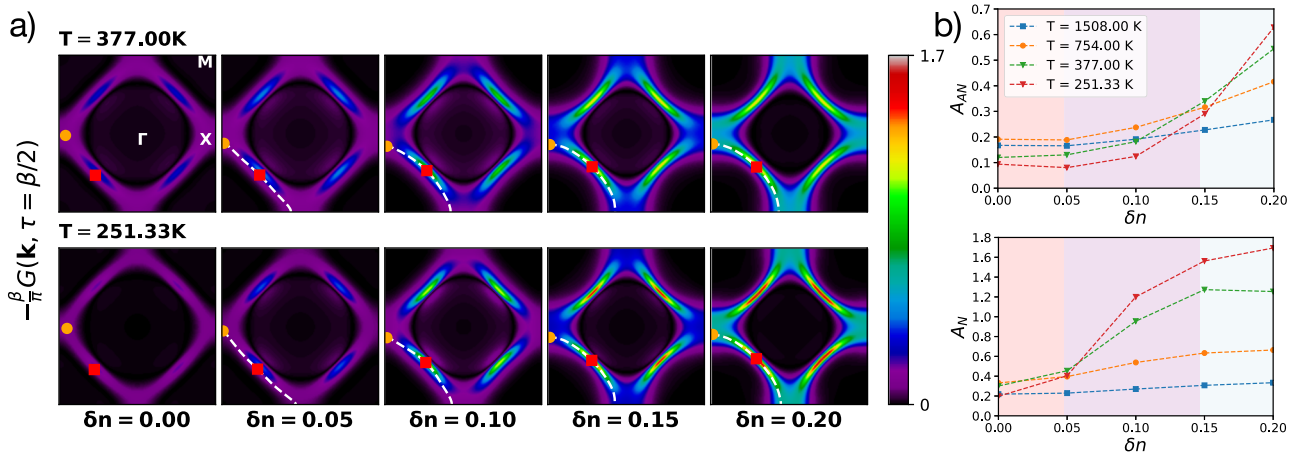

Fig. 2 | Hole-doping evolution of DΓA spectral function at the Fermi energy and at the nodal and anti-nodal points. a Hole-doping evolution of DΓA **k**-resolved spectral intensities at the Fermi energy for $T = t_{pp}/20 = 377$ K (upper panels) and $T = t_{pp}/30 = 251.33$ K (lower panels) with displayed interacting Fermi plus Luttinger surface (dashed white line) and the position of the nodal (red square) and anti-nodal (orange circle) points. **b** Hole-doping and temperature dependence of the spectral function at the interacting Fermi surface at the nodal (upper panel) and anti-nodal (lower panel) points. The shaded background highlights the different crossovers revealed by DΓA, indicated in Fig. 1 by the same color.

surface determined by ARPES[15,62,63] evolves similarly to our calculations: at small dopings the spectral weight is low and concentrated around the node, while the Fermi arcs enlarge at intermediate doping, before the Fermi surface eventually closes at $\delta n \approx 0.2$, indicating the rise and fall of the pseudogap. In addition, in the pseudogap phase, the doping and temperature dependence of the nodal point displays a metallic behavior, while the antinodal point only becomes metallic above certain doping values, $\delta n = 0.15$ in our calculation. This is also in good agreement with the electronic Raman scattering experiments[65] for Bi-2212, where the same behavior is reported but with an "optimal" doping at $\delta n = 0.2$. Furthermore, in the overdoped regime ($\delta n \geq 0.3$), the emergence of the inverse Lifshitz transition in our calculations agrees well with ARPES[62,63,66] and transport measurements[67] in LSCO, as well as with electronic Raman spectroscopy[68–70] for Bi-2212.

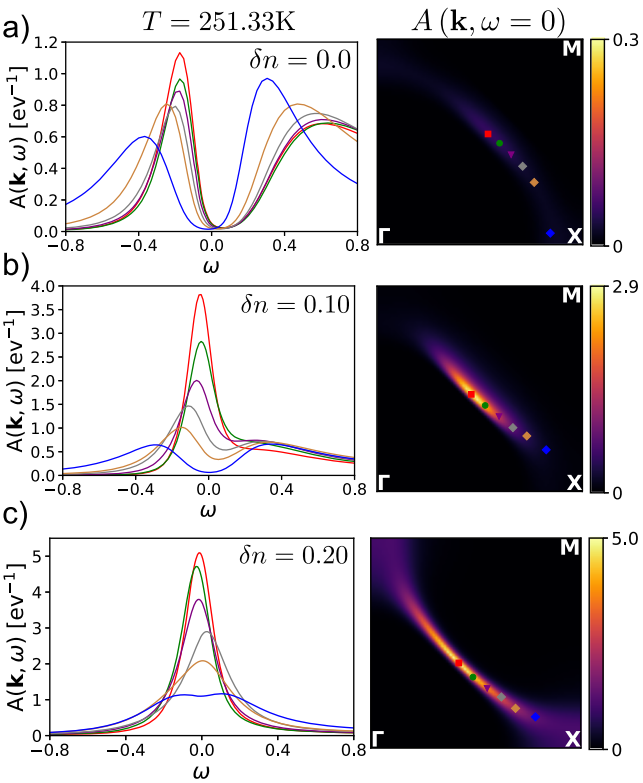

Fig. 3 | Hole doping evolution of the electronic spectral function over the Fermi surface. Hole-doping evolution of the low-frequency behavior of the electronic spectral function (left panel) at points along the Fermi surface (right panel) T = 251.33 K ($\beta t_{pp} = 30$), in the **a** insulating ($\delta n = 0.00$), **b** pseudogap ($\delta n = 0.10$), and **c** metallic ($\delta n = 0.20$) regime. The local spectral functions were obtained by MaxEnt analytical continuation[50].

Regarding magnetism, a crossover from commensurate to incommensurate magnetic fluctuations has been observed in inelastic neutron scattering experiments for LSCO[71,72]. There, the onset of incommensurability has already been determined to start at very low doping levels, with a direct proportionality of incommensurability and hole doping[72]. Our computational results instead have a non-zero doping threshold for incommensurate fluctuations, which we attribute to the lower temperatures $T \lesssim 40$ K, at which the experiments have been performed. Let us note that incommensurability has also been measured in $YBa_2Cu_3O_{6+x}$[73], however, it seems to be absent in $HgBa_2CuO_{4+\delta}$[74].

The (in-plane) magnetic correlation length ξ has been shown to significantly drop from about 15 lattice spacings in LSCO near the parent compound, to about 3-4 lattice spacings for $\delta n \in [0.05, 0.15]$[75], being in very good agreement with our calculations in the pseudogap regime. In addition, the presence of short-ranged magnetic fluctuations in the pseudogap regime ($0.05 < \delta n < 0.15$) is also in good agreement with electronic Raman spectroscopy experiments[76] for Bi-2212.

Regarding the NMR response, in the pseudogap regime, our calculations demonstrate the downturn of the uniform spin susceptibility upon cooling, which was historically interpreted as the onset of the pseudogap phase[20,77]. A similar behavior has also been shown for $La_{2-x}Sr_xCuO_4$[78] in SQUID magnetometry measurements. Concerning the overall increase in the magnitude of $\chi_{sp}(\mathbf{0}, 0)$ with increasing doping, our computational results agree well with a wide range of materials, including $La_{2-x}Sr_xCuO_4$[78,79] and YBa_2CuO_{7-x}[80], where the same trend is observed.

Let us finally comment that an in-depth comparison between the Emery and the Hubbard model is beyond the scope of our present work. If the respective models could be solved exactly, we expect that qualitative and quantitative differences in their results would in principle stem from (i) explicit multiorbital physics (e.g., charge orders involving both the copper and oxygen sites[81]), (ii) higher-energy processes like flavors of charge-transfer excitations, and (iii) the mixed-orbital character of the resulting band structure. On the other hand, for low-energy quantities (such as Fermi surfaces and static response functions), we expect a smaller difference. This would explain the good agreement between the phenomenology of the

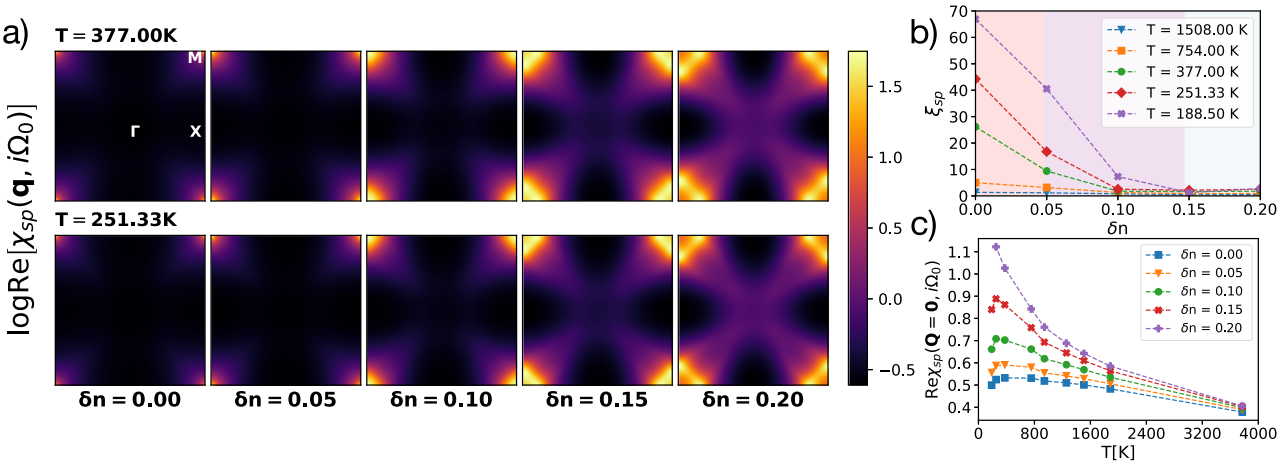

Fig. 4 | Hole-doping and temperature evolution of DΓA lattice two-particle observables. a Hole-doping evolution of the logarithm of the q-resolved ladder DΓA static spin susceptibility for $T = 377$ K (upper panels) and $T = 251.33$ K (lower panels). **b** Hole-doping and temperature dependence of ladder DΓA spin correlation length. **c** Temperature evolution of the uniform magnetic lattice susceptibility $\chi(\mathbf{0}, 0)$: $-\chi(\mathbf{0}, i\Omega_n = 0)$ for different hole-doping levels.

Emery model in ladder-DΓA presented in the main text and the calculations on the single-band Hubbard model[10,21–26].

Conclusions

With ladder DΓA calculations, we have demonstrated that the Emery model captures the rise and fall of the pseudogap through a series of crossovers from the insulating to the pseudogap to the metallic regime. Our results are in good agreement with the signatures of the normal phase observed in spectroscopic experiments for cuprates. Both the insulating and pseudogap phases are accompanied by (short-range) commensurate antiferromagnetic correlations, while the metallic state is dominated by incommensurate ones. The short-ranged nature of these fluctuations characterize the emerging pseudogap as being of strong-coupling type. Establishing these key features for the normal phase of the fundamental model for cuprates, the three-band Emery model, represents a step towards the universal theoretical description of cuprates.

Data availability

Relevant data supporting the findings are publicly available at https://doi.org/10.17617/3.VLMSCF.

Code availability

DMFT and ladder DΓA calculations were performed with the TRIQS library, which is publicly available at: https://triqs.github.io/triqs/latest/

Received: 7 October 2025; Accepted: 6 May 2026;
Published online: 19 May 2026

References

1. Bednorz, J. G. & Müller, K. A. Possible high T_c superconductivity in the Ba-La-Cu-O system. *Z. f.ür. Phys. B Condens. Matter* **64**, 189–193 (1986).
2. Keimer, B., Kivelson, S. A., Norman, M. R., Uchida, S. & Zaanen, J. From quantum matter to high-temperature superconductivity in copper oxides. *Nature* **518**, 179–186 (2015).
3. Zaanen, J., Sawatzky, G. A. & Allen, J. W. Band gaps and electronic structure of transition-metal compounds. *Phys. Rev. Lett.* **55**, 418–421 (1985).
4. Zhang, F. C. & Rice, T. M. Effective Hamiltonian for the superconducting Cu oxides. *Phys. Rev. B* **37**, 3759–3761 (1988).
5. Emery, V. J. Theory of high-T_c superconductivity in oxides. *Phys. Rev. Lett.* **58**, 2794–2797 (1987).
6. Varma, C., Schmitt-Rink, S. & Abrahams, E. Charge transfer excitations and superconductivity in "ionic" metals. *Solid State Commun.* **62**, 681–685 (1987).
7. Andersen, O., Liechtenstein, A., Jepsen, O. & Paulsen, F. LDA energy bands, low-energy Hamiltonians, $t\prime$, t'', $t_\perp(k)$, and $J_\perp$. *J. Phys. Chem. Solids* **56**, 1573–1591 (1995).
8. Li, D. et al. Superconductivity in an infinite-layer nickelate. *Nature* **572**, 624–627 (2019).
9. Kitatani, M. et al. Nickelate superconductors—a renaissance of the one-band Hubbard model. *npj Quantum Mater.* **5**, 59 (2020).
10. Klett, M., Hansmann, P. & Schäfer, T. Magnetic properties and pseudogap formation in infinite-layer nickelates: Insights from the single-band Hubbard model. *Front. Phys.* **10**, 834682 (2022).
11. Qin, M., Schäfer, T., Andergassen, S., Corboz, P. & Gull, E. The Hubbard model: a computational perspective. *Annu. Rev. Condens. Matter Phys.* **13**, 275–302 (2022).
12. Arovas, D. P., Berg, E., Kivelson, S. A. & Raghu, S. The Hubbard Model. *Annu. Rev. Condens. Matter Phys.* **13**, 239–274 (2022).
13. Damascelli, A., Hussain, Z. & Shen, Z.-X. Angle-resolved photoemission studies of the cuprate superconductors. *Rev. Mod. Phys.* **75**, 473–541 (2003).
14. Kanigel, A. et al. Evolution of the pseudogap from Fermi arcs to the nodal liquid. *Nat. Phys.* **2**, 447–451 (2006).
15. Yoshida, T. et al. Systematic doping evolution of the underlying Fermi surface of $La_{2-x}Sr_xCuO_4$. *Phys. Rev. B* **74**, 224510 (2006).
16. Shen, K. M. et al. Nodal quasiparticles and antinodal charge ordering in $Ca_{2-x}Na_xCuO_2Cl_2$. *Science* **307**, 901–904 (2005).
17. Taillefer, L. Scattering and pairing in cuprate superconductors. *Annu. Rev. Condens. Matter Phys.* **1**, 51–70 (2010).
18. Boschini, F. et al. Emergence of pseudogap from short-range spin-correlations in electron-doped cuprates. *npj Quantum Mater.* **5**, 6 (2020).
19. Boschini, F., Zonno, M. & Damascelli, A. Time-resolved ARPES studies of quantum materials. *Rev. Mod. Phys.* **96**, 015003 (2024).
20. Alloul, H., Ohno, T. & Mendels, P. ^{89}Y NMR evidence for a fermi-liquid behavior in $YBa_2Cu_3O_{6+x}$. *Phys. Rev. Lett.* **63**, 1700–1703 (1989).
21. Kyung, B., Hankevych, V., Daré, A.-M. & Tremblay, A.-M. S. Pseudogap and spin fluctuations in the normal state of the electron-doped cuprates. *Phys. Rev. Lett.* **93**, 147004 (2004).
22. Wu, W. et al. Pseudogap and Fermi-Surface topology in the two-dimensional Hubbard model. *Phys. Rev. X* **8**, 021048 (2018).
23. Schäfer, T. et al. Tracking the footprints of spin fluctuations: a multimethod, multimessenger study of the two-dimensional Hubbard model. *Phys. Rev. X* **11**, 011058 (2021).
24. Krien, F., Worm, P., Chalupa-Gantner, P., Toschi, A. & Held, K. Explaining the pseudogap through damping and antidamping on the Fermi surface by imaginary spin scattering. *Commun. Phys.* **5**, 336 (2022).
25. Vilk, Y. M., Lahaie, C. & Tremblay, A.-M. S. Antiferromagnetic pseudogap in the two-dimensional Hubbard model deep in the renormalized classical regime. *Phys. Rev. B* **110**, 125154 (2024).
26. Šimkovic, F., Rossi, R., Georges, A. & Ferrero, M. Origin and fate of the pseudogap in the doped Hubbard model. *Science* **385**, eade9194 (2024).
27. Avella, A., Mancini, F., Mancini, F. P. & Plekhanov, E. Emery vs. Hubbard model for cuprate superconductors: a composite operator method study. *Eur. Phys. J. B* **86**, 265 (2013).
28. Fratino, L., Sémon, P., Sordi, G. & Tremblay, A.-M. S. Pseudogap and superconductivity in two-dimensional doped charge-transfer insulators. *Phys. Rev. B* **93**, 245147 (2016).
29. Dash, S. S. & Sénéchal, D. Pseudogap transition within the superconducting phase in the three-band Hubbard model. *Phys. Rev. B* **100**, 214509 (2019).
30. Mao, T. & Jiang, M. Non-Fermi liquid behavior of scattering rate in three-orbital Emery model (2024). arXiv: 2403.11218
31. Gauvin-Ndiaye, C. et al. Two-particle self-consistent approach for multiorbital models: Application to the Emery model. *Phys. Rev. B* **109**, 165111 (2024).
32. Sordi, G., Reaney, G. L., Kowalski, N., Sémon, P. & Tremblay, A. M. S. Ambipolar doping of a charge-transfer insulator in the Emery model (2024). arXiv: 2407.19545
33. Bacq-Labreuil, B., Lacasse, B., Tremblay, A.-M. S., Sénéchal, D. & Haule, K. Towards an ab initio theory of high-temperature superconductors: a study of multilayer cuprates (2024). arXiv: 2410.10019
34. Mai, P., Cohen-Stead, B., Maier, T. A. & Johnston, S. Fluctuating charge-density-wave correlations in the three-band Hubbard model. *Proc. Natl. Acad. Sci.* **121**, e2408717121 (2024).
35. Kowalski, N., Dash, S. S., Sémon, P., Sénéchal, D. & Tremblay, A.-M. Oxygen hole content, charge-transfer gap, covalency, and cuprate superconductivity. *Proc. Natl. Acad. Sci. USA* **118**, e2106476118 (2021).
36. Mai, P., Balduzzi, G., Johnston, S. & Maier, T. A. Orbital structure of the effective pairing interaction in the high-temperature superconducting cuprates. *npj Quantum Mater.* **6**, 26 (2021).
37. Mai, P., Balduzzi, G., Johnston, S. & Maier, T. A. Pairing correlations in the cuprates: a numerical study of the three-band Hubbard model. *Phys. Rev. B* **103**, 144514 (2021).

38. Galler, A., Thunström, P., Gunacker, P., Tomczak, J. M. & Held, K. Ab initio dynamical vertex approximation. *Phys. Rev. B* **95**, 115107 (2017).
39. Weber, C., Yee, C., Haule, K. & Kotliar, G. Scaling of the transition temperature of hole-doped cuprate superconductors with the charge-transfer energy. *Europhys. Lett.* **100**, 37001 (2012).
40. Tseng, Y.-T. et al. Single-particle spectra and magnetic susceptibility in the Emery model: a dynamical mean-field perspective. *SciPost Phys.* **18**, 145 (2025).
41. Bocquet, A. E., Mizokawa, T., Saitoh, T., Namatame, H. & Fujimori, A. Electronic structure of 3d-transition-metal compounds by analysis of the 2p core-level photoemission spectra. *Phys. Rev. B* **46**, 3771–3784 (1992).
42. Bocquet, A. E. et al. Electronic structure of early 3d-transition-metal oxides by analysis of the 2p core-level photoemission spectra. *Phys. Rev. B* **53**, 1161–1170 (1996).
43. Toschi, A., Katanin, A. A. & Held, K. Dynamical vertex approximation; a step beyond dynamical mean-field theory. *Phys. Rev. B* **75**, 045118 (2007).
44. Rohringer, G. et al. Diagrammatic routes to nonlocal correlations beyond dynamical mean field theory. *Rev. Mod. Phys.* **90**, 025003 (2018).
45. Georges, A., Kotliar, G., Krauth, W. & Rozenberg, M. J. Dynamical mean-field theory of strongly correlated fermion systems and the limit of infinite dimensions. *Rev. Mod. Phys.* **68**, 13 (1996).
46. Maier, T., Jarrell, M., Pruschke, T. & Hettler, M. H. Quantum cluster theories. *Rev. Mod. Phys.* **77**, 1027–1080 (2005).
47. Kitatani, M., Arita, R., Schäfer, T. & Held, K. Strongly correlated superconductivity with long-range spatial fluctuations. *J. Phys.Mater.* **5**, 034005 (2022).
48. Meixner, M. et al. Mott transition and pseudogap of the square-lattice Hubbard model: Results from center-focused cellular dynamical mean-field theory. *SciPost Phys.* **16**, 059 (2024).
49. Kitatani, M. et al. Optimizing superconductivity: from cuprates via nickelates to palladates. *Phys. Rev. Lett.* **130**, 166002 (2023).
50. Reymbaut, A., Gagnon, A.-M., Bergeron, D. & Tremblay, A.-M. S. Maximum entropy analytic continuation for frequency-dependent transport coefficients with nonpositive spectral weight. *Phys. Rev. B* **95**, 121104 (2017).
51. Ye, M., Wang, Z., Fernandes, R. M. & Chubukov, A. V. Location and thermal evolution of the pseudogap due to spin fluctuations. *Phys. Rev. B* **108**, 115156 (2023).
52. Ye, M. & Chubukov, A. V. Crucial role of thermal fluctuations and vertex corrections for the magnetic pseudogap. *Phys. Rev. B* **108**, L081118 (2023).
53. Gunnarsson, O. et al. Fluctuation diagnostics of the electron self-energy: origin of the pseudogap Physics. *Phys. Rev. Lett.* **114**, 236402 (2015).
54. Wu, W., Ferrero, M., Georges, A. & Kozik, E. Controlling Feynman diagrammatic expansions: physical nature of the pseudogap in the two-dimensional Hubbard model. *Phys. Rev. B* **96**, 041105(R) (2017).
55. Schäfer, T. & Toschi, A. How to read between the lines of electronic spectra: the diagnostics of fluctuations in strongly correlated electron systems. *J. Phys.: Condens. Matter* **33**, 214001 (2021).
56. Mermin, N. D. & Wagner, H. Absence of ferromagnetism or antiferromagnetism in one- or two-dimensional isotropic Heisenberg models. *Phys. Rev. Lett.* **17**, 1307–1307 (1966).
57. Mila, F. & Rice, T. Analysis of magnetic resonance experiments in $YBa_2Cu_3O_7$. *Phys. C: Superconduct.* **157**, 561–570 (1989).
58. Shastry, B. S. t-J model and nuclear magnetic relaxation in high-T_c materials. *Phys. Rev. Lett.* **63**, 1288–1291 (1989).
59. Zhou, R. et al. Signatures of two gaps in the spin susceptibility of a cuprate superconductor. *Nat. Phys.* **21**, 97–103 (2025).
60. Alloul, H. What do we learn from impurities and disorder in high-T_c cuprates? *Front. Phys.* **12**, 1406242 (2024).
61. Yoshida, T. et al. Universal versus material-dependent two-gap behaviors of the high-T_c cuprate superconductors: angle-resolved photoemission study of $La_{2-x}Sr_xCuO_4$. *Phys. Rev. Lett.* **103**, 037004 (2009).
62. Matt, C. E. et al. Electron scattering, charge order, and pseudogap physics in $la_{1.6-x}nd_{0.4}sr_xcuo_4$: An angle-resolved photoemission spectroscopy study. *Phys. Rev. B* **92**, 134524 (2015).
63. Chang, J. et al. Anisotropic quasiparticle scattering rates in slightly underdoped to optimally doped high-temperature $la_{2-x}sr_xcuo_4$ superconductors. *Phys. Rev. B* **78**, 205103 (2008).
64. Cyr-Choinière, O. et al. Pseudogap temperature T^* of cuprate superconductors from the Nernst effect. *Phys. Rev. B* **97**, 064502 (2018).
65. Venturini, F. et al. Observation of an unconventional metal-insulator transition in overdoped cuo_2 compounds. *Phys. Rev. Lett.* **89**, 107003 (2002).
66. Ino, A. et al. Doping-dependent evolution of the electronic structure of $la_{2-x}sr_xcuo_4$ in the superconducting and metallic phases. *Phys. Rev. B* **65**, 094504 (2002).
67. Doiron-Leyraud, N. et al. Pseudogap phase of cuprate superconductors confined by Fermi surface topology. *Nat. Commun.* **8**, 2044 (2017).
68. Loret, B. et al. Vertical temperature boundary of the pseudogap under the superconducting dome in the phase diagram of $bi_2sr_2cacu_2o_{8+\delta}$. *Phys. Rev. B* **96**, 094525 (2017).
69. Loret, B. et al. Raman and ARPES combined study on the connection between the existence of the pseudogap and the topology of the Fermi surface in $bi_2sr_2cacu_2o_{8+\delta}$. *Phys. Rev. B* **97**, 174521 (2018).
70. Benhabib, S. et al. Collapse of the normal-state pseudogap at a Lifshitz transition in the $bi_2sr_2cacu_2o_{8+\delta}$ cuprate superconductor. *Phys. Rev. Lett.* **114**, 147001 (2015).
71. Birgeneau, R. J. et al. Static and dynamic spin fluctuations in superconducting $La_{2-x}Sr_xCuO_4$. *Phys. Rev. B* **39**, 2868–2871 (1989).
72. Yamada, K. et al. Doping dependence of the spatially modulated dynamical spin correlations and the superconducting-transition temperature in $La_{2-x}Sr_xCuO_4$. *Phys. Rev. B* **57**, 6165–6172 (1998).
73. Haug, D. et al. Neutron scattering study of the magnetic phase diagram of underdoped $YBa_2Cu_3O_{6+x}$. *N. J. Phys.* **12**, 105006 (2010).
74. Anderson, Z. W. et al. Gapped commensurate antiferromagnetic response in a strongly underdoped model cuprate superconductor (2024). arXiv: 2412.03524
75. Birgeneau, R. J. et al. Antiferromagnetic spin correlations in insulating, metallic, and superconducting $La_{2-x}Sr_xCuO_4$. *Phys. Rev. B* **38**, 6614–6623 (1988).
76. Mezidi, M. et al. Spin singlet and quasiparticle excitations in cuprate superconductors. *Phys. Rev. B* **106**, 174513 (2022).
77. Takigawa, M. et al. Cu and o nmr studies of the magnetic properties of yba_2 cu_3 $o_{6.63}$ (t_c=62 k). *Phys. Rev. B* **43**, 247–257 (1991).
78. Ohsugi, S., Kitaoka, Y., Ishida, K., Zheng, G. -q & Asayama, K. Cu nmr and nqr studies of high-t c superconductor la2-xsrxcuo4. *J. Phys. Soc. Jpn.* **63**, 700–715 (1994).
79. Nakano, T. et al. Magnetic properties and electronic conduction of superconducting la_{2-x} sr_x cuo_4. *Phys. Rev. B* **49**, 16000–16008 (1994).
80. Barzykin, V. & Pines, D. Magnetic scaling in cuprate superconductors. *Phys. Rev. B* **52**, 13585–13600 (1995).
81. Uchida, S. et al. Optical spectra of La_{2-x} Sr_x CuO_4: Effect of carrier doping on the electronic structure of the CuO_2 plane. *Phys. Rev. B* **43**, 7942–7954 (1991).

Acknowledgements

We acknowledge fruitful discussions with Nils Wentzell, Paul Worm and Patrick Tscheppe on the theoretical and numerical part of our work, as well as with Eva Benckiser and Matthias Hepting on experiments on cuprates and critical reading of our manuscript. The work has been supported in part by the Austrian Science Funds (FWF) through Grant DOI 10.55776/I5398.

We further acknowledge financial support by the DFG project HA7277/3-1. This research was also supported by the Deutsche Forschungsgemeinschaft (DFG, German Research Foundation) through the research unit QUAST through FOR 5249 through DFG ID No. 449872909 (P4) and FWF project DOI 10.55776/I5868 (P1). The authors appreciate the scientific support and HPC resources provided by the Erlangen National High Performance Computing Center (NHR@FAU) of the Friedrich-Alexander-Universität Erlangen-Nüürnberg (FAU) [hardware funded by the German Research Foundation—DFG], and the computing service facility of the MPI-FKF, responsible for the Bordeaux cluster.

Author contributions

M.O.M. performed the ladder DΓA computations presented in the manuscript. H.M. and Y.T. performed the single-particle DMFT calculations. E.J. provided benchmark data for the DΓA calculations. T.S., P.H., and K.H. supervised the work. All authors contributed to the discussion of the results and the preparation of the manuscript.

Funding

Open Access funding enabled and organized by Projekt DEAL.

Competing interests

The authors declare no competing interests.

Additional information

Supplementary information The online version contains supplementary material available at https://doi.org/10.1038/s42005-026-02685-6.

Correspondence and requests for materials should be addressed to M. O. Malcolms or Thomas Schäfer.

Peer review information *Communications Physics* thanks Alexey Rubtsov, Giovanni Mirarchi and the other, anonymous, reviewer for their contribution to the peer review of this work. A peer review file is available.

Reprints and permissions information is available at http://www.nature.com/reprints

Publisher's note Springer Nature remains neutral with regard to jurisdictional claims in published maps and institutional affiliations.

Open Access This article is licensed under a Creative Commons Attribution 4.0 International License, which permits use, sharing, adaptation, distribution and reproduction in any medium or format, as long as you give appropriate credit to the original author(s) and the source, provide a link to the Creative Commons licence, and indicate if changes were made. The images or other third party material in this article are included in the article's Creative Commons licence, unless indicated otherwise in a credit line to the material. If material is not included in the article's Creative Commons licence and your intended use is not permitted by statutory regulation or exceeds the permitted use, you will need to obtain permission directly from the copyright holder. To view a copy of this licence, visit http://creativecommons.org/licenses/by/4.0/.

© The Author(s) 2026